INL/JOU-22-70455-Revision-0

Porous potassium tantalate-reduced graphene oxide nano cube architecture for high performance hybrid supercapacitors

June 2023

Kunal Mondal, Apurva Nandagudi, Sumedha H. Nagarajarao, Shivaraj B Patil, V.G. Dileep Kumar, M. S. Santosh, Ankur Gupta, Basavanakote M. Basavaraja

INL/JOU-22-70455-Revision-0

Porous potassium tantalate-reduced graphene oxide nano cube architecture for high performance hybrid supercapacitors

Kunal Mondal, Apurva Nandagudi, Sumedha H. Nagarajarao, Shivaraj B Patil, V.G. Dileep Kumar, M. S. Santosh, Ankur Gupta, Basavanakote M. Basavaraja

June 2023

Idaho National Laboratory
Idaho Falls, Idaho 83415

http://www.inl.gov

e-Prime - Advances in Electrical Engineering, Electronics and Energy 4 (2023) 100182

Contents lists available at ScienceDirect

e-Prime - Advances in Electrical Engineering, Electronics and Energy

journal homepage: www.elsevier.com/locate/prime

Porous potassium tantalate-reduced graphene oxide nano cube architecture for high performance hybrid supercapacitors

Apurva Nandagudi [a], Sumedha H. Nagarajarao [b], Shivaraj B. Patil [c], V.G. Dileep Kumar [a,d], M.S. Santosh [d,e], Ankur Gupta [f], Kunal Mondal [g,h,i], Basavanakote M. Basavaraja [a,*]

[a] Department of Chemistry (Science and Humanities), PES University, 100 Ft. Ring Road, BSK 3rd Stage, Bengaluru, 560085, India
[b] Department of Chemistry, College of Engineering and Technology, Srinivas University, Mukka, Mangalore, 574146, India
[c] Department of Chemistry, Tunghai University, Taichung 40704, Taiwan
[d] Coal to Hydrogen Energy for Sustainable Solutions (CHESS) Division, CSIR - Central Institute of Mining and Fuel Research (CIMFR), Digwadih Campus, PO: FRI, Dhanbad - 828108, Jharkhand, India
[e] Academy of Scientific and Innovative Research (AcSIR), Ghaziabad, 201 002, India
[f] Department of Mechanical Engineering, Indian Institute of Technology, Jodhpur, India
[g] Materials Science and Engineering Department, Idaho National Laboratory, Idaho Falls, ID 83415, United States
[h] Department of Civil & Environmental Engineering, Idaho State University, Pocatello, ID 83209, United States
[i] Nuclear Energy and Fuel Cycle Division, Oak Ridge National Laboratory, 1 Bethel Valley Road, Oak Ridge, TN 37830, United States

ARTICLE INFO

Keywords:
$KTaO_3$
rGO
Nano cubes
Chronopotentiometry
Hybrid supercapacitor

ABSTRACT

Energy storage has always been a major concern in the present-day situation. Advanced energy storage devices are batteries, supercapacitor and solar cells. However, advancements have been noteworthy in the field of high-performance hybrid supercapacitors. On this note, we have fabricated a hybrid supercapacitor electrode material Potassium tantalate nano cube (KT NCs) and its reduced graphene oxide composite (KT-rGO NCs) and tested its electrochemical performance. The materials showed high performances with specific capacitance of 565 F/g for KT NCs and 850 F/g for KT-rGO NCs respectively. Energy densities of both KT NCs & KT-rGO NCs are 28.24 Wh/Kg and 29.50 Wh/kg with good retention capacities. Further detailed study of both KT NCs and KT-rGO NCs are carried out with characterization techniques like XRD, FTIR, BET, Raman and HRTEM for structural analysis and electrochemical measurements to analyse various parameters pertaining to its charge storage capacity.

1. Introduction

A rise in the energy demand has accorded to the need of extensive research in the field of advanced materials for supercapacitor applications [1–4]. This also comes with the challenges in terms of efficiency, energy storage and other environmental concerns during its disposal. Applications of a supercapacitor are tremendous beginning with the military to various techniques in automotive industries. Sooner or later supercapacitors (SCs) have reached a vital stage where it can be a conventional battery [5–7].

Supercapacitors can be differentiated into electrochemical double layer capacitors (EDLCs) and Pseudo capacitors (battery-type), in which the former stores energy in the electrode/electrolyte interface and the latter by fast and reversible faradaic reactions at the surface of electrode. At present, the combination of both EDLCs and Pseudo capacitors play a vital role in fulfilling the high-energy needs with good stability. In hybrid SCs, the electrodes comprise both transition metal oxides (TMOs) and carbon material. However, structural degradation is one of the basic limitations in a faradaic reaction. This can be evaded using carbon materials such as highly porous carbon, carbon aerogels, carbon nanofibers, carbon nanotubes (CNTs), graphene etc. along with the electrode, which is advantageous in its fabrication and workability at a wide temperature range [8–11].

A transition metal oxide nanocomposite material is used in the electrodes of the SCs to match to the advanced high energy needs. So far, highly used materials in SCs include various TMOs such as TiO_2, Ru_2O, ZnO, NiO, V_2O_5, Fe_2O_3 etc. [12–14]. The exhibition of EDLCs essentially relies upon the kinds of the anode materials used. As of late, a few kinds of carbon materials have been accounted for EDLCs, for example, porous carbons, nanofibers of carbon, carbide-determined carbons (CDCs),

---

[*] Corresponding author.
E-mail address: bmbasavaraja@gmail.com (B.M. Basavaraja).

https://doi.org/10.1016/j.prime.2023.100182
Received 27 February 2023; Received in revised form 18 May 2023; Accepted 29 May 2023
Available online 30 May 2023

templated carbons, nanotubes of carbon, and graphene. Amongst these, graphene is one of the additional promising competitors for EDLC in view of its mechanical strength, high surface area, high conductivity, and flexibility [15–18].

Tantalum oxide is widely used in readily available supercapacitors with real-time applications. It can also be extended in the field of advanced energy storage in hybrid supercapacitors. Furthermore, Potassium tantalate is a well-known perovskite electrode material because of its simple cubic structure, high mobility [19] and pseudo capacitance which adds up to the performance of a supercapacitor. Further, it has been used in superconducting interfacial studies and photocatalytic applications too. Liu et.al. Have worked on the anisotropic transport at $KTaO_3$ interfaces [20]. Sumedha et.al have synthesized $KTaO_3$ using novel method and used in photocatalysis, hydrogen evolution reactions (HER) and oxygen evolution reactions (OER) with good efficiency and high performances [21].

Our research group is also involved in the preparation of TMOs like ZnO, ZnO/PANI composite and ZnO/rGO composite and other such materials and their advanced applications in lithium batteries and electrochemical sensors in detection of various analytes [22–27]. Comparative studies of various perovskite materials and the present material are shown in Table 1.

Herein, we have synthesized potassium tantalate nanocubes (KT NCs) and potassium tantalate-rGO (KT-rGO NCs) composite by a hydrothermal approach adapting areca nut powder as the carbon source. The prepared materials are utilised in supercapacitor studies and have displayed better electrochemical performance in comparison to a bare metal oxide. As per our knowledge, this is the first time that cubic potassium tantalate perovskite and its reduced graphene oxide composite have been used in high performance supercapacitor applications.

2. Materials and methods

2.1. Preparation of areca seed powder

Areca seeds were extracted from Sringeri, Sringeri taluk, Chikkamagaluru district, Karnataka, India. The collected seeds are cleaned with distilled water for a few times, dried, powdered into 100-mesh size and was stored at normal temperature.

2.2. Preparation of KT NCs

Solution combustion method was adopted using areca seed extract as the fuel. Tantalum (V) oxide (Ta_2O_5) and potassium hydroxide (KOH) were obtained from sigma Aldrich (AR) and have been used as procured. Areca seed extract and 0.4 g of tantalum oxide were pulverised for 15 min with the aid of an agate mortar. Hence prepared solid was transferred to a clean dry crucible, after which 1.4 M KOH solution was added and stirred for 15 min and then subjected to calcination at 700 °C in a muffle furnace pre-heated at 500 °C for 10 min. Milky white coloured powder of potassium tantalate nanoparticles were obtained and stored in an airtight desiccator for further use.

Table 1
Comparative studies of various perovskite materials and the present material

Material	Specific capacitance (Fg^{-1})	Energy density (Wh Kg^{-1})	Power density (W Kg^{-1})	Reference
$LaNiO_3$	106.58	–	–	[42]
$La_{0.85}Sr_{0.15}MnO_3$	186	20.6	1700	[43]
$MoO_3/Au/MoO_3$	275	24.5	377	[44]
$LaFeO_3$	241.3	34	900	[45]
$SrMnO_3$	446.8	37	400	[46]
$KTaO_3$-rGO NCs	850	29.5	17,000	Present work

2.3. Preparation of KT-rGO NCs

100 mg of graphene oxide was dispersed for 30 min in distilled water, to which 200 mg of prepared potassium tantalate nanoparticles are added. This solution was later sonicated for 10 min, later, which it was placed in a hot air oven for hydrothermal reaction at 180 °C for 24 h. After the reaction, the suspension was kept for drying at 70 °C for 24 h. Hence, obtained solid composite was crushed using a pestle and mortar and stored for analysis.

2.4. Fabrication of electrodes

Uniformly dispersed KT NCs is added to a mixture of water and ethanol (1:1) and sonicated for 10 min. Then about 0.90 µl of Nafion was added to the solution and sonicated. This solution was coated on a nickel foam measuring 1.5 cm height and 1 cm width. Ni foam was coated with drop-wise addition of the solution leaving the top portion. It was then dried completely and used as an electrode.

Further, KT-rGO NCs is also coated in the same way and utilised for electrochemical studies.

2.5. Electrochemical measurements

All electrochemical studies of KT NCs and KT-rGO NCs are recorded through Charge-discharge (Chronopotentiometry), cyclic voltammogram (CV) and Impedance (EIS) by using CH-660E instrument at 20°C. The KT NCs/Ni electrode and KT-rGO NCs/Ni electrode acts as a working electrode, saturated calomel electrode and platinum electrode were operated as a reference and counter electrodes in a 3-electrode system respectively. For electrochemical measurements, 0.1 M KOH electrolyte was taken with scan rates of 1–100 mV/s and 1–10 Ag^{-1} current densities with 100 kHz-1 Hz frequency range. The charge-discharge curve was used to calculate the specific capacitance of KT NCs and KT-rGO NCs using Eq. (1) given below.

$$Csp = \frac{I \times \Delta t}{m \times \Delta V} \tag{1}$$

In the above equation, specific capacitance (Csp) measured in Fg^{-1}, Current (I) in mA, discharge time (Δt) in seconds, amount of active material (m) in mg and operational window (ΔV) in V.

2.6. Material characterization

Phase of the material synthesized was determined by Philips X'pert-PRO diffractometer (Cu-Kα, $\lambda = 1.5418$ Å) with scan speed of 2° min^{-1}, 10–80° as its 2θ range to obtain X-ray diffraction data, PerkinElmer FTIR (Spectrum-1000) spectrometer in the range of 4000–400 cm^{-1} was used in FTIR analysis. Quanta Chrome Nova 2200e Surface Area & Pore Size analyser Nova station A is being used for BET surface area calculations. Morphology at the surface was measured using High-resolution transmission electron microscope (HRTEM) (Jeol/JEM 2100 200 kV). Varied oxidation states were determined using X-ray photoelectron spectroscopy (XPS) (Kratos Axis Ultra DLD instrument equipped with a monochromatic Al Kα X-ray source). Structural analysis was carried out using VESTA software. CH 660E potentiostat (CH Instruments, USA) and the cyclic voltammograms (CV) were used to carry out different electrochemical measurements of the material which were noted by employing a three-electrode system, having working electrode (Ni foam), counter electrode (platinum wire) and reference electrodes (Calomel electrode). Electrochemical studies were performed with 0.1 M KOH as the electrolyte at varied scan rates (1–100 mV/s), with a raise of 10 mV, in the potential range of −0.6 to 1.2 V (vs reference electrode). The impedance measurements were verified between the frequency range of 1 Hz to 1 MHz having 5 mV AC amplitude.

3. Results

3.1. Powder X-ray diffraction studies: (P-XRD)

Fig. 1 shows the powder X-ray diffractometer (PXRD) studies of both KT NCs and KT-rGO NCs ranging from 15 to 80° θ. The obtained highly intense peaks were well matched with the JCPDS card no-38–1470 and 38–8745 for KT NCs and KT-rGO NCs respectively with negligible impurity peaks. The hkl values for KT NCs were found to be at (100), (110), (111), (200), (210), (211), (220), (300), (310), (311), (222), (320) planes with highly pure and intense peaks.

Perovskites generally have the cubic crystal lattice in the form of ABO_3. High thermal resistance is one of the major advantages of tantalum oxide, but under certain conditions, this might change. The prepared KT-rGO NCs showed similar hkl values as that of the KT NCs with slight shift in their positions and intensities. Yet another important observation is that there is a change in phase when potassium tantalate is processed through hydrothermal reaction as majority of the perovskites are sensitive to thermal treatments [28].

Debye-Scherer's equation is utilised to calculate the average crystalline size of both KT NCs and KT-rGO NCs and found to be between 20 and 25 nm. Crystal defect may be the main reason behind the less crystallite size of KT NCs.

$$D = \frac{K\lambda}{\beta \, Cos \, \theta} \tag{2}$$

Using the Eq. (2), d spacing can be determined. In the above equation, Crystallite Shape Constant (0.89) is K, Wavelength of X ray beam is noted as λ, Cu-Kα radiation (1.5406 Å), β-Full width at half maximum (FWHM) and θ being the diffraction angle.

Crystal structure has been shown in Fig. 1c exhibiting the ABO_3 structure of perovskite. It shows that all the lattice parameters a, b and c are equal to 3.98830 and α, β and γ at 90° Its unit cell volume was found to be 63.440 $Å^3$. Transport properties of perovskites depend upon their defects in the crystal lattice leading to good ionic conductivities [3]. Thus, slight distortions in their electrochemical performances can be observed when doped with a carbon.

3.2. Fourier transform infrared spectroscopy (FTIR)

The bonding characteristics of potassium, tantalum and oxygen were measured and given in Fig. 2 For KT-rGO NCs, the most intense peak was detected at 610 cm^{-1} exhibiting bond between Ta and O (Ta-O) [29] and medium intense peak at 1400 cm^{-1} corresponds to the C—H bending frequency and C═C vibrations which corresponds to 1641 cm^{-1} may be from the amount of fuel added [30]. The peak at 3422 cm^{-1}, confirmed the adsorption of moisture or water. For KT-rGO NCs, characteristic reduced graphene oxide (rGO) peak was observed at 1570 cm^{-1} which incurs the formation of rGO [31]. Further, the presence of rGO in KT-rGO NCs was confirmed with the help of Raman spectroscopy.

3.3. Raman spectroscopy

Prepared perovskites were further characterized using Raman spectroscopy primarily for the identification of crystal structure. Fig. 3 shows Raman peak positions at 237, 600 and 810 cm^{-1} correspond to the perovskite structure of potassium tantalate. Characteristic bands between 100 and 500 cm^{-1} accounts for O—Ta—O bending vibrations and that of 500–900 cm^{-1} for Ta—O bonds with unequal bond strengths [32]. Further, carbon peaks at 1033 and 1286 cm^{-1} can be directed towards usage of carbon source in fuel [33]. Presence of rGO has been intensified in the bands 1356 and 1580 cm^{-1} which corresponds to D-Band and G-band [34]. A D-band is derived from the C—C stretching and G due to the aromatic rings. Further, Id/Ig ratio for the rGO band was found to be 0.926 and looking into the intensities of D and G band we can infer that there has been low reduction with high degree of disorder in the material [33].

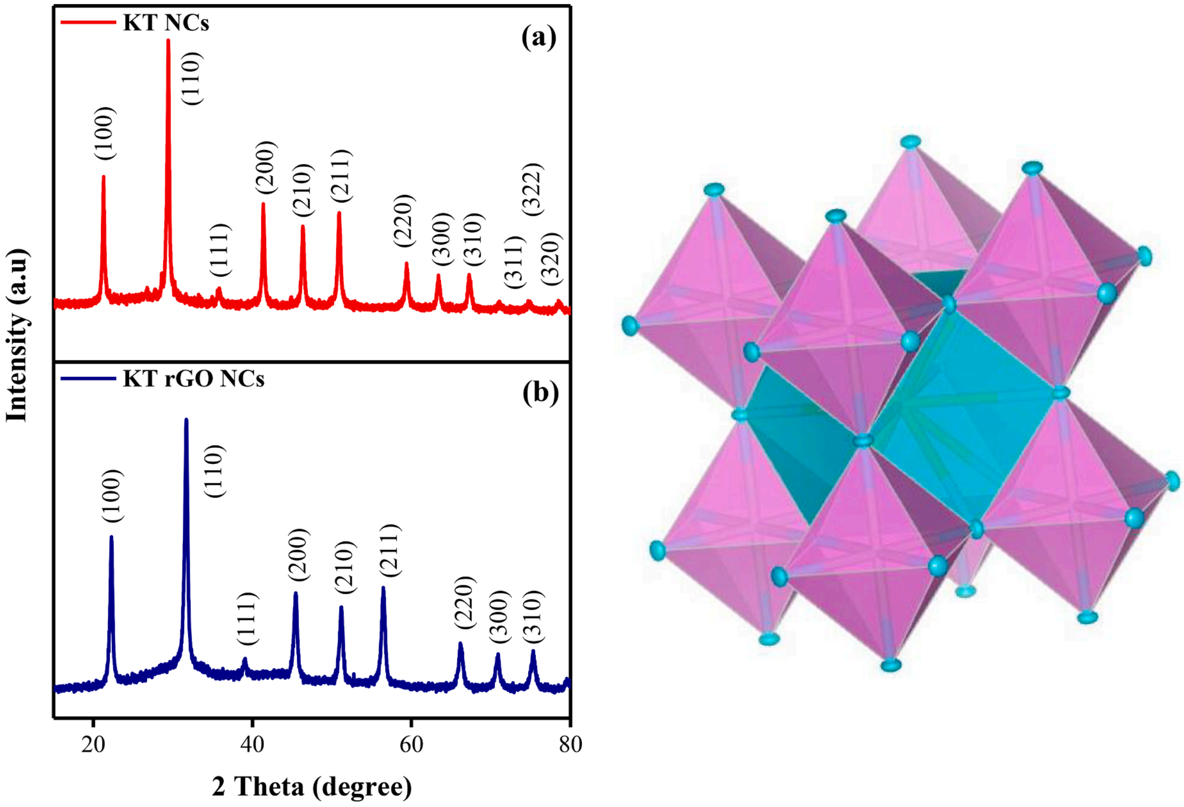

Fig. 1. XRD pattern of (a) KT NCs, (b) KT-rGO NCs and Crystal structure of KT NCs.

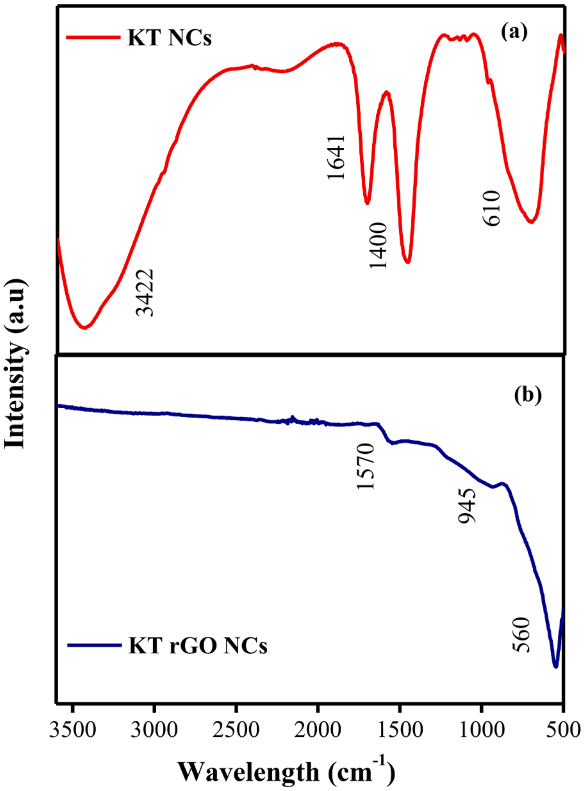

Fig. 2. FTIR spectrum of (a) KT NCs and (b) KT-rGO NCs.

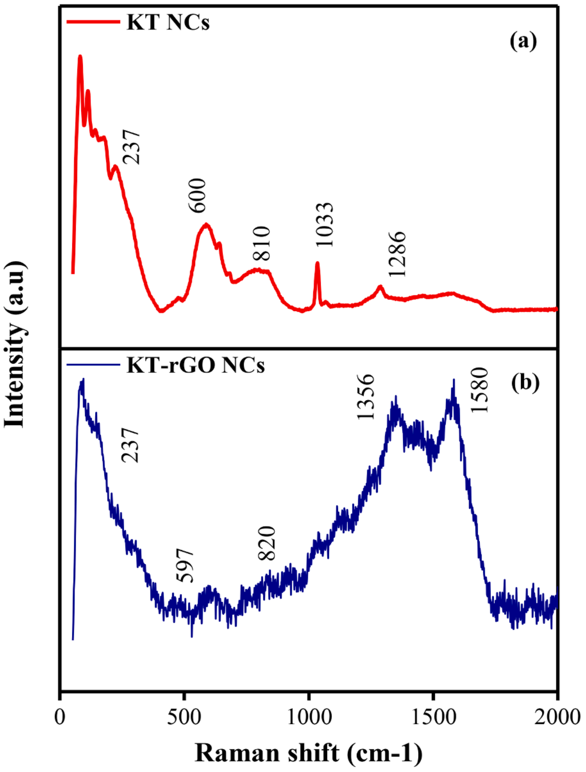

Fig. 3. Raman spectra of (a) KT NCs and (b) KT- rGO NCs.

3.4. *Transmission electron microscopy (TEM)*

The images obtained from different magnifications of HRTEM technique were shown in Fig. 4. The d spacing of KT and rGO-KT from HRTEM images found to be 0.38 nm and 0.68 nm respectively. KT NCs have been attached to rGO sheets as shown in the Fig. 4d making it slight distorted. This contact permits the electronic collaboration between KT NCs and rGO sheets and could be possibly valuable for successful detachment of charge transporters. The SAED patterns have been shown in 4c and 4f, which correlates, to KT NCs and KT-rGO NCs. The hkl values of both KT NCs and KT-rGO NCs correlate to that of its JCPDS card numbers.

3.5. *BET surface area analysis*

Surface area of a particle can be easily scrutinized using BET Nitrogen adsorption-desorption curves. The mesoporous nature of both KT NCs and KT-rGO NCs are confirmed by hysteresis loop of type IV isotherm curve shown in Fig. 5a. The KT-rGO NCs exhibit more BET surface area of 4.37 m^2g^{-1} compared to 2.534 m^2g^{-1} of bare KT NCs. The mean pore diameter and total pore volume of KT NCs were 3.106 nm and 0.009 m^3g^{-1} respectively, whereas the complement values of KT-rGO NCs were 5.03 nm and 0.012 m^3g^{-1}. The more diffusion of OH^- ions of electrolyte through electrode surface takes place by increase in both surface area and pore volume of material. The pore size distribution curves in BJH (Barrett-Joyner-Halenda) plot exhibits almost similar values for both KT NCs and KT-rGO NCs shown in Fig. 5b.

3.6. *XPS studies: (X-ray photoelectron spectroscopy)*

Composition of KT NCs and KT-rGO NCs elemental characteristics can be uniquely verified with X-ray photoelectron spectroscopy.

The fitted spectra of K 2p, Ta 4f, O 1 s and C 1 s spectra are depicted in the Fig. 6. This explains the presence of elements potassium, tantalum, oxygen and carbon respectively. The carbon peak at 286.2 eV ascribes to C—C bond. The Ta 4f exhibits two states of Ta $4f_{7/2}$ at 26.3 eV and Ta $4f_{5/2}$ at 28.2 eV. K 2p line consists of a peak at 291.5 and 294 eV which attributes to K $2p_{3/2}$ and K $2p_{1/2}$ with higher intensity for $KTaO_3$ crystal lattice. O 1 s spectra reveals a doublet at 531.5 eV and 533.6 eV corresponding to carbonyl oxygen and hydroxy oxygen respectively [35, 36]. Thus, obtained different oxidation state of the metal indicates the amount of metal ions available for the redox reaction and its electrochemical performance.

3.7. *Electrochemical studies*

Cyclic voltammetry

The CV technique is adopted to analyse the specific capacitance of both KT NCs and KT-rGO NCs at potential window 0 to 0.8 V. Initially both coated nickel foams were stabilised for 20 cycles at 20 mV/s and later CV studies were employed at varied scan rates from 1 mV/s to 100 mV/s. The formula to calculate the specific capacitance from CV studies is given below in Eq. (3) [37].

$$Cs = \frac{Current\,(A)}{Active\,mass\,(g) * Potential\ window\,(V) * Scan\ rate\,(V/S)}\ Fg^{-1} \qquad (3)$$

The cyclic voltammogram of KT NCs and KT-rGO NCs at different scan rates were recorded and depicted in Fig. 7a and 7b respectively.

It can be noted that, the CV curve of KT-rGO NCs has more area compared to bare KT NCs, which can be correlated to its enhanced charge storage capacity. A capacitance of 571 F/g was achieved for KT-rGO NCs whereas KT NCs exhibits a capacitance of 489 F/g at 10 mV/s scan rate. Pseudocapacitive behaviour of these Nano cubes is detected by the typical redox shape with clear indication of anodic and cathodic peaks in Fig. 7a. It was recognised that, KT NCs has comparatively less (0.15 V) anodic and cathodic potential difference (E_a-E_c) than that of KT-

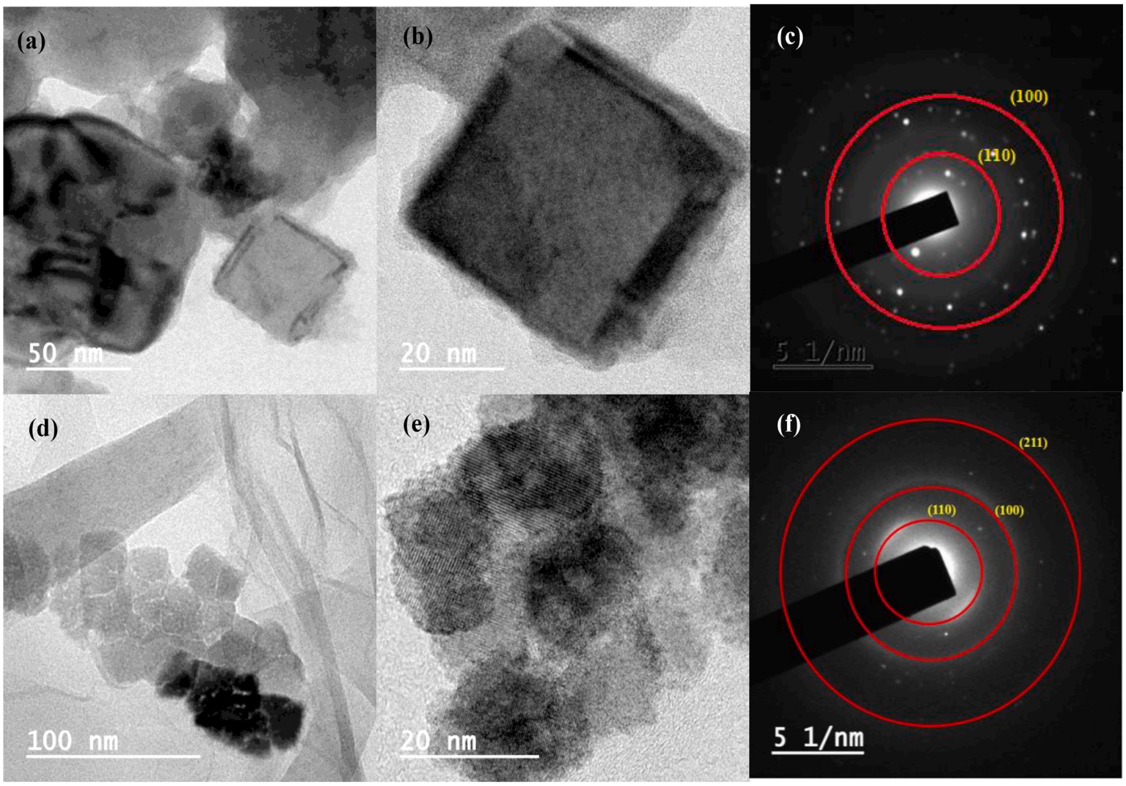

Fig. 4. HRTEM images of KT NCs (a and b) with its SAED pattern (c) and that of KT-rGO NCs (d and e) with corresponding SAED pattern (f).

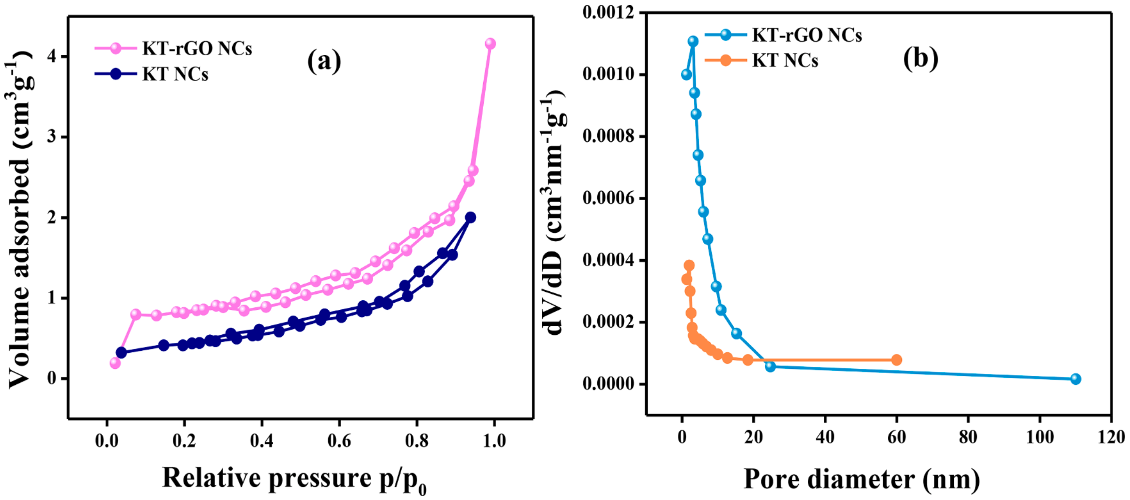

Fig. 5. (a) Nitrogen adsorption-desorption isotherm of KT NCs and KT-rGO NCs and (b) BJH pore size distribution of KT NCs and KT-rGO NCs.

rGO NCs (0.18 V), which proves the good reversibility of pseudocapacitive reaction [38].

It is confirmed that with higher scan rates, the anodic peaks move towards greater voltage and cathodic peaks towards lesser voltage values. In addition, capacitance fall was observed on increase in scan rates. The diffusion of OH^- ions will be more in lesser scan rates, which leads to increase in the capacitance. The specific capacitance for KT NCs and KT-rGO NCs were found to be 449, 398, 350, 256, 150 and 571, 450, 410, 310, 240 F/g at scan rates 1, 10, 30, 50, 100 mV/s respectively.

3.8. Galvanostatic charge discharge

At different current densities (1–5 A/g), the GCD studies were done for both KT NCs and KT-rGO NCs shown in Fig. 8a and 8b. The higher potential of 0.5 V was observed for KT NCs, whereas 0.45 V for KT-rGO NCs. The specific capacitance using charge-discharge curve was calculated by the formula given in Eq. (4).

$$Cs = \frac{Discharge\ time\ (s) * Current\ density\ (Ag^{-1})}{Active\ mass\ (g) * Potential\ window\ (V)}\ Fg^{-1} \tag{4}$$

The specific capacitance calculated using CV curves were of 850 and 565 F/g was recorded for KT-rGO NCs and KT NCs respectively. The discharge curves of both KT NCs and KT-rGO NCs at current density of 1 A/g were depicted in supplementary information. The discharge pattern was observed to be the combination of both pseudocapacitive and electrical double layer capacitive behaviour of materials. Specific

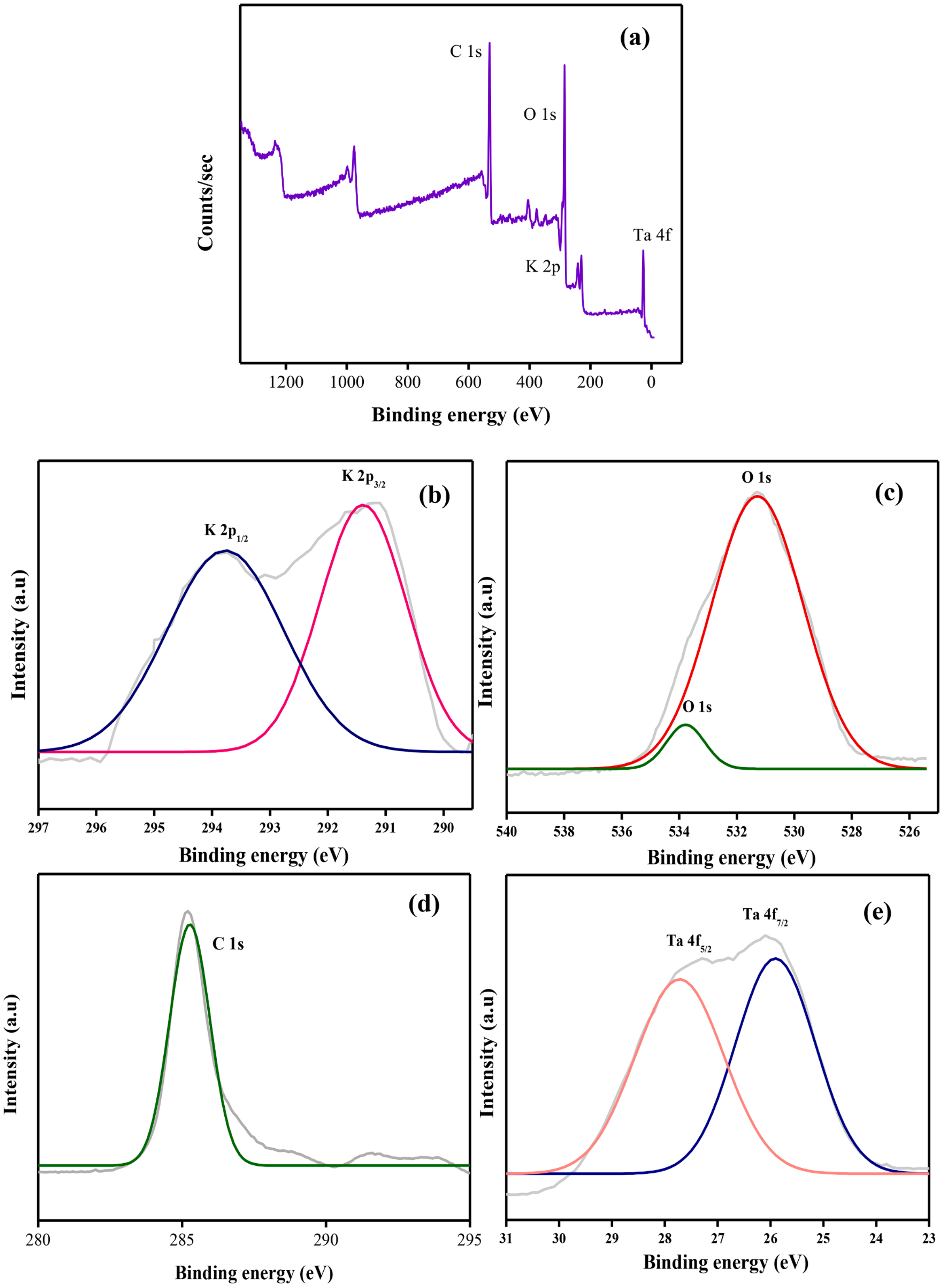

Fig. 6. XPS survey spectrum of KT-rGO NCs (a), XPS spectra of K 2p (b), O 1 s (c), C 1 s (d) and Ta 4f (e).

capacitance calculated with the help of Eq. (4) using the charge-discharge curves were 60 F/g for KT NCs and 136 F/g for KT-rGO NCs at a constant current density of 1 A/g with retention of 62% and 73% after 6600 cycles. Energy density of bare KT NCs were found to be 28.24 Wh/Kg and KT-rGO NCs was 29.50 Wh/Kg at the constant current density of 1 A/g.

Resistance offered by an electrode material is analysed using AC Impedance studies. Nyquist plot in Fig. 8d provides an electrochemical impedance spectroscopy in comparison to both KT NCs and KT-rGO NCs before and after charge-discharge cycles. Minimum charge-transfer resistance leads to good capacitance and vice versa. This adds to the overall Ohmic resistance, which includes resistance due to the electrolyte, solvent and current collector. Smaller semicircle indicates less ion transfer resistance and wider indicates more [39]. Thus, carbon composite has offered less ohmic resistance, with improved performance. Further, addition of rGO helps in the enhancement of the active sites

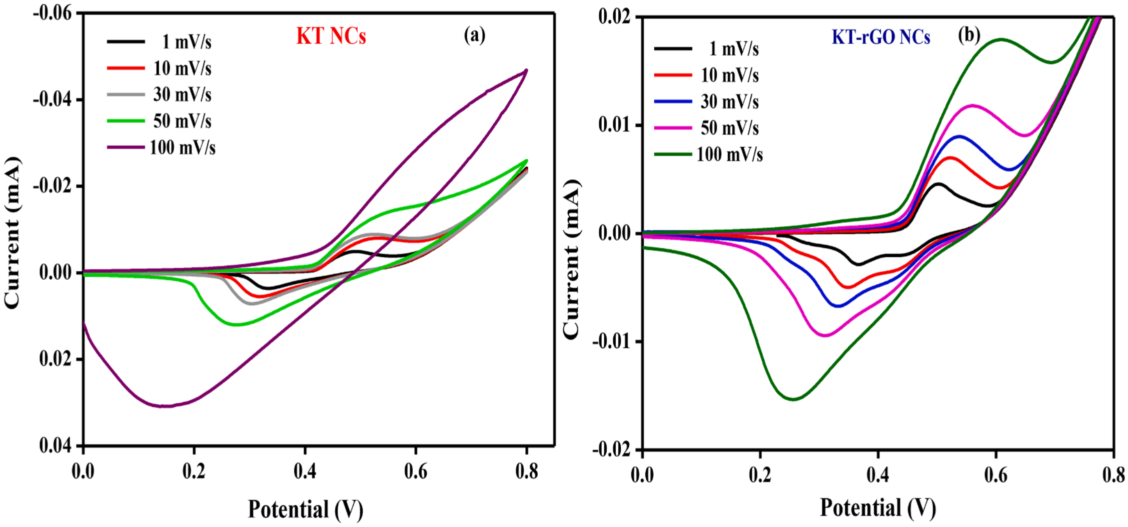

Fig. 7. Cyclic voltammetry curves of (a) KT NCs and (b) KT-rGO NCs.

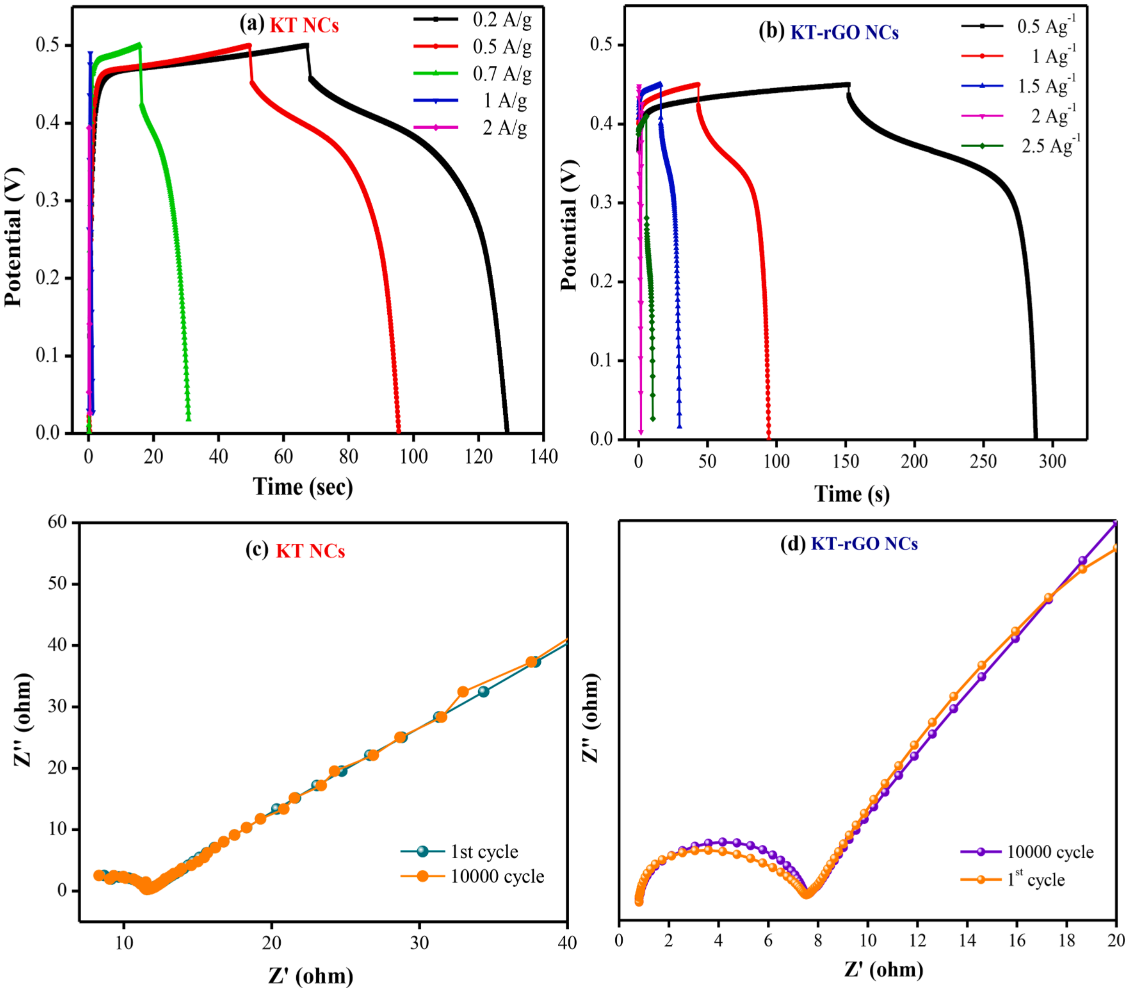

Fig. 8. Galvanostatic charge-discharge studies – (a) GCD curves of KT NCs, (b) GCD curves of KT-rGO NCs and Nyquist plots for both KT NCs and KT-rGO NCs in 0.1 M KOH electrolyte.

available for the redox reaction and high porosity leads to easy movement of charges offering minimum resistance [40,41].

These results demonstrate that the addition of a carbon matrix such as reduced graphene oxide enhances the strength, flexibility, and efficiency of the electrode material. Present work portrays the fundamentals of design and fabrication of carbon-based porous composites with high performance and their use in applications like thin films. This advanced material can be a potentially suitable electrode material in high performance hybrid supercapacitor electrodes.

4. Discussion & conclusion

In the present study, we have correlated the enhanced performances between potassium tantalate and its reduced graphene oxide composite with respect to various electrochemical characterizations. Potassium tantalate nanocubes were synthesized by a solution combustion approach with a novel carbon source (areca seed extract) and thus obtained KT NCs were used in KT-rGO NCs synthesis. Reduced Graphene oxide composite has exhibited high performance with good stability, low charge transfer resistance and high specific capacitance of 850 F/g at 1 A/g and a higher power density of 17,000 W/Kg when compared to the bare material at 9000 W/Kg. Energy density of bare KT NCs were found to be 28.24 Wh/Kg and KT-rGO NCs were 29.50 Wh/Kg at the constant current density of 1 A/g. Thus, usage of perovskite $KTaO_3$ material and addition of carbonaceous matrix can be used as a promising hybrid supercapacitor device.

Declaration of Competing Interest

The authors declare that they have no known competing financial interests or personal relationships that could have appeared to influence the work reported in this paper.

Data availability

Data will be made available on request.

Acknowledgements

Authors thank the Department of Chemistry, Mysore University, for providing FTIR and Raman spectroscopy data. K.M. would like to sincerely acknowledge the support received from the Energy and Environment Science and Technology department at the Idaho National Laboratory, USA. Furthermore, K.M. extends heartfelt acknowledgement to the distinguished Oak Ridge National Laboratory, USA, for their generous support.

Supplementary materials

Supplementary material associated with this article can be found, in the online version, at doi:10.1016/j.prime.2023.100182.

References

[1] R. Kumar, et al., An overview of recent progress in nanostructured carbon-based supercapacitor electrodes: from zero to bi-dimensional materials, Carbon N.Y. 193 (2022) 298–338, https://doi.org/10.1016/j.carbon.2022.03.023.

[2] R. Wang, et al., Metal/metal oxide nanoparticles-composited porous carbon for high-performance supercapacitors, J. Energy Storage 38 (2021), 102479, https://doi.org/10.1016/j.est.2021.102479.

[3] S. Kaur, et al., Unraveling the dependency on multiple passes in laser-induced graphene electrodes for supercapacitor and H2O2 sensing, Mater. Sci. Energy Technol. 4 (2021) 407–412, https://doi.org/10.1016/j.mset.2021.09.004.

[4] Y.L. Oliveira, et al., Investigation of electronic structure, morphological features, optical, colorimetric, and supercapacitor electrode properties of CoWO4 crystals, Mater. Sci. Energy Technol. 5 (2022) 125–144, https://doi.org/10.1016/j.mset.2021.12.006.

[5] S. Najib, E. Erdem, Current progress achieved in novel materials for supercapacitor electrodes: mini review, Nanoscale Adv. 1 (8) (2019) 2817–2827, https://doi.org/10.1039/C9NA00345B.

[6] Poonam, et al., Review of supercapacitors: materials and devices, J. Energy Storage 21 (2019) 801–825, https://doi.org/10.1016/j.est.2019.01.010.

[7] D.P. Chatterjee, A.K. Nandi, A review on the recent advances in hybrid supercapacitors, J. Mater. Chem. A 9 (29) (2021) 15880–15918, https://doi.org/10.1039/D1TA02505H.

[8] D.M. El-Gendy, N.A. Abdel Ghany, N.K. Allam, Black titania nanotubes/spongy graphene nanocomposites for high-performance supercapacitors, RSC Adv. 9 (22) (2019) 12555–12566, https://doi.org/10.1039/C9RA01539F.

[9] M. Zhi, et al., Nanostructured carbon–metal oxide composite electrodes for supercapacitors: a review, Nanoscale 5 (1) (2013) 72–88, https://doi.org/10.1039/C2NR32040A.

[10] C. Zhong, et al., A review of electrolyte materials and compositions for electrochemical supercapacitors, Chem. Soc. Rev. 44 (21) (2015) 7484–7539, https://doi.org/10.1039/C5CS00303B.

[11] Y. Deng, et al., Review on recent advances in nitrogen-doped carbons: preparations and applications in supercapacitors, J. Mater. Chem. A 4 (4) (2016) 1144–1173, https://doi.org/10.1039/C5TA08620E.

[12] M.I. da Silva, et al., Recent progress in water-splitting and supercapacitor electrode materials based on MOF-derived sulfides, J. Mater. Chem. A 10 (2) (2022) 430–474, https://doi.org/10.1039/D1TA05927K.

[13] X.-y. Luo, Y. Chen, Y. Mo, A review of charge storage in porous carbon-based supercapacitors, New Carbon Mater. 36 (1) (2021) 49–68, https://doi.org/10.1016/S1872-5805(21)60004-5.

[14] M. Gheytanzadeh, et al., Insights into the estimation of capacitance for carbon-based supercapacitors, RSC Adv. 11 (10) (2021) 5479–5486, https://doi.org/10.1039/D0RA09837J.

[15] D. A, G. Hegde, Activated carbon nanospheres derived from bio-waste materials for supercapacitor applications – a review, RSC Adv. 5 (107) (2015) 88339–88352, https://doi.org/10.1039/C5RA19392C.

[16] M. Sevilla, R. Mokaya, Energy storage applications of activated carbons: supercapacitors and hydrogen storage, Energy Environ. Sci. 7 (4) (2014) 1250–1280, https://doi.org/10.1039/C3EE43525C.

[17] P.-L. Taberna, et al., Activated carbon–carbon nanotube composite porous film for supercapacitor applications, Mater. Res. Bull. 41 (3) (2006) 478–484, https://doi.org/10.1016/j.materresbull.2005.09.029.

[18] D. Yang, C. Bock, Laser reduced graphene for supercapacitor applications, J. Power Sources 337 (2017) 73–81, https://doi.org/10.1016/j.jpowsour.2016.10.108.

[19] E. Rezaie, A. Hajalilou, Y. Su, Perovskites for Supercapacitors. Handbook of Supercapacitor Materials, 2021, pp. 131–185.

[20] C. Liu, et al., Two-dimensional superconductivity and anisotropic transport at $KTaO_3$(111) interfaces, Science 371 (6530) (2021) 716–721, https://doi.org/10.1126/science.aba5511.

[21] H.N. Sumedha, et al., Novel 3D-flower shaped KTaO3 perovskite for highly efficient photocatalytic and H2 generation ability, Sci. Rep. 12 (1) (2022) 10776, https://doi.org/10.1038/s41598-022-14590-3.

[22] Shilpa, et al., Electrospun hollow glassy carbon–reduced graphene oxide nanofibers with encapsulated ZnO nanoparticles: a free standing anode for Li-ion batteries, J. Mater. Chem. A 3 (10) (2015) 5344–5351, https://doi.org/10.1039/C4TA07220K.

[23] O.J. D`Souza, et al., Platinum decorated multi-walled carbon nanotubes/Triton X-100 modified carbon paste electrode for the sensitive amperometric determination of Paracetamol, J. Electroanal. Chem. 739 (2015) 49–57, https://doi.org/10.1016/j.jelechem.2014.12.012.

[24] G. Manasa, et al., An electrochemical Bisphenol F sensor based on ZnO/G nano composite and CTAB surface modified carbon paste electrode architecture, Colloids Surf. B 170 (2018) 144–151, https://doi.org/10.1016/j.colsurfb.2018.06.002.

[25] O.J. D`Souza, et al., A novel ZnO/reduced graphene oxide and Prussian blue modified carbon paste electrode for the sensitive determination of Rutin, Sci. China Chem. 62 (2) (2019) 262–270, https://doi.org/10.1007/s11426-018-9353-x.

[26] M. G, R.J. Mascarenhas, B.M. Basavaraja, Sensitively-selective determination of Propyl Paraben preservative based on synergistic effects of polyaniline-zinc-oxide nano-composite incorporated into graphite paste electrode, Colloids Surf. B 184 (2019), 110529, https://doi.org/10.1016/j.colsurfb.2019.110529.

[27] S.H. Nagarajarao, et al., Recent developments in supercapacitor electrodes: a mini review, ChemEng. 6 (1) (2022) 5.

[28] E.A.R. Assirey, Perovskite synthesis, properties and their related biochemical and industrial application, Saudi Pharm. J. 27 (6) (2019) 817–829, https://doi.org/10.1016/j.jsps.2019.05.003.

[29] B. Bajorowicz, et al., Perovskite-type KTaO3–reduced graphene oxide hybrid with improved visible light photocatalytic activity, RSC Adv. 5 (111) (2015) 91315–91325, https://doi.org/10.1039/C5RA18124K.

[30] L. Tong, et al., Normal and abnormal dielectric relaxation behavior in KTaO3 ceramics, RSC Adv. 7 (80) (2017) 50680–50687, https://doi.org/10.1039/C7RA09866A.

[31] T.F. Emiru, D.W. Ayele, Controlled synthesis, characterization and reduction of graphene oxide: a convenient method for large scale production, Egypt. J. Basic Appl. Sci. 4 (1) (2017) 74–79, https://doi.org/10.1016/j.ejbas.2016.11.002.

[32] A. Krukowska, et al., Mono- and bimetallic nanoparticles decorated KTaO3 photocatalysts with improved Vis and UV–Vis light activity, Appl. Surf. Sci. 441 (2018) 993–1011, https://doi.org/10.1016/j.apsusc.2018.02.077.

[33] V. Scardaci, G. Compagnini, Raman spectroscopy investigation of graphene oxide reduction by laser scribing, C 7 (2) (2021) 48.

[34] C.R. Minitha, R.T. Rajendrakumar, Synthesis and characterization of reduced graphene oxide, Adv. Mat. Res. 678 (2013) 56–60, https://doi.org/10.4028/www.scientific.net/AMR.678.56.

[35] C. Meng, et al., Hydrothermal preparation of novel rGO-KTaO3 nanocubes with enhanced visible light photocatalytic activity, Spectrochim. Acta Part A 250 (2021), 119352, https://doi.org/10.1016/j.saa.2020.119352.

[36] X. Lu, et al., Fabrication of a novel BiOI/KTaO3 p–n heterostructure with enhanced photocatalytic performance under visible-light irradiation, RSC Adv. 10 (18) (2020) 10921–10931, https://doi.org/10.1039/C9RA10231K.

[37] M. Ramani, et al., Synthesis and characterization of hydrous ruthenium oxide-carbon supercapacitors, J. Electrochem. Soc. 148 (4) (2001) A374, https://doi.org/10.1149/1.1357172.

[38] L.L. Zhang, Z. Xiong, X.S. Zhao, A composite electrode consisting of nickel hydroxide, carbon nanotubes, and reduced graphene oxide with an ultrahigh electrocapacitance, J. Power Sources 222 (2013) 326–332, https://doi.org/10.1016/j.jpowsour.2012.09.016.

[39] H.D. Yoo, et al., Impedance analysis of porous carbon electrodes to predict rate capability of electric double-layer capacitors, J. Power Sources 267 (2014) 411–420, https://doi.org/10.1016/j.jpowsour.2014.05.058.

[40] Q. Ke, J. Wang, Graphene-based materials for supercapacitor electrodes – A review, J. Materiomics 2 (1) (2016) 37–54, https://doi.org/10.1016/j.jmat.2016.01.001.

[41] L. Miao, et al., Recent advances in carbon-based supercapacitors, Mater. Adv. 1 (5) (2020) 945–966, https://doi.org/10.1039/D0MA00384K.

[42] N. Arjun, G.-T. Pan, T.C.K. Yang, The exploration of Lanthanum based perovskites and their complementary electrolytes for the supercapacitor applications, Results Phys. 7 (2017) 920–926, https://doi.org/10.1016/j.rinp.2017.02.013.

[43] X. Lang, et al., Ag nanoparticles decorated perovskite La0.85Sr0.15MnO3 as electrode materials for supercapacitors, Mater. Lett. 243 (2019) 34–37, https://doi.org/10.1016/j.matlet.2019.02.002.

[44] F. Zhou, et al., Perovskite photovoltachromic supercapacitor with all-transparent electrodes, ACS Nano 10 (6) (2016) 5900–5908, https://doi.org/10.1021/acsnano.6b01202.

[45] Y. Zhang, et al., Mesoporous LaFeO3 perovskite derived from MOF gel for all-solid-state symmetric supercapacitors, Chem. Eng. J. 386 (2020), 124030, https://doi.org/10.1016/j.cej.2020.124030.

[46] G. George, et al., Effect of doping on the performance of high-crystalline SrMnO3 perovskite nanofibers as a supercapacitor electrode, Ceram. Int. 44 (17) (2018) 21982–21992, https://doi.org/10.1016/j.ceramint.2018.08.313.